Applying Kondo Physics?

Z. Fisk

UC Irvine

Supported by NSF

Can what we learned from 4f Kondo systems be useful in transition metal materials?

- Origin of Kondo physics
- Kondo -> dense Kondo
- Intermediate valence
- 4f to 5f
- Kondo insulators
- Zintl compounds

History of Kondo effect

- transition metal impurities in simple metals
- Solubility question
- depression of T_c

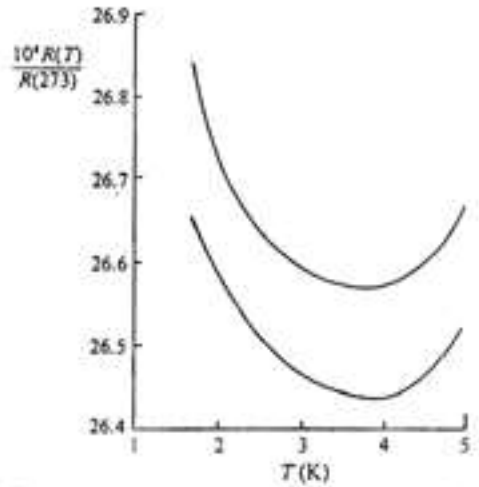

Figure 1 The minimum in the electrical resistivity of *Au* (de Haas, de Boer and van den Berg, 1934).

3d transition metal impurities such as *Fe*, dependent on the impurity concentration.

The resistance minimum as observed in *Au* is shown in figure 1, reproduced from the 1953 edition of *The Theory of Metals* by A.H. Wilson, one of the standard texts of this period. The reason for the minimum was not known at that time and Wilson comments, 'the cause of the minimum is entirely obscure and constitutes a most striking departure from Mathiessens's rule, according to which the ideal and residual resistances are additive — some new physical principle seems to be involved'. A very significant advance in the theory of magnetic impurities was an explanation of this effect by J. Kondo in 1964.

Early theoretical work on impurities in metals in the late 50s by J. Friedel and associates concentrated on explaining the trends in the behaviour as the impurity elements are varied across the transition element series. The most important concept to emerge from this work was that of 'virtual bound states' ; states which are almost localized due to resonant scattering at the impurity site. A different formulation of this idea was put forward by P.W. Anderson (1963), in a version now known as the 'Anderson model': this model has played a very important role in

of the transition temperature with valence electron concentration. However, the maxima for the magnetic-moment plot coincide with the minima for the transition-temperature plot.

An interesting case is the depression of the transition temperature of Ru by the addition of small amounts of Cr, up to 20 at. % Cr, which also seems to be due to a magnetic interaction. For higher concentrations of Cr the magnetic interaction disappears, as had been observed in the Cr-Fe system, and for Ru solid solutions containing more than 30 at. % Cr the variation in transition temperature with composition is in accord with the empirical rules.[111]

The effect of magnetic rare-earth elements on the superconducting transition temperature of La has been investigated in detail.[104,112] The lowering of the transition temperature by the rare-earth element seems to be correlated chiefly with the projection of the spin on the orbit of the solute atoms and not with an increase of the effective moment.[104] The effective magnetic moments and spins of the rare-earth elements follow Van Vleck's[113] well-known curve, given in Fig. 2. The superconducting transition temperatures of solid solutions of La containing 1 at. % of rare-earth element are shown in Fig. 3. It was also concluded from these studies that the depression was essentially symmetrical with respect to Gd. The results of additional studies indicate that a deviation from the symmetrical behavior occurs in La–Nd and in La–Er solid solutions.[112] The transition temperature of La is lowered much more rapidly by Nd than by Er. Both elements have the same spin but the effective magnetic moment of Er is much larger than that of Nd. Here again a larger effective moment increases the transition temperature rather than decreasing it. Theoretical calculations[114,115] which attribute the lowering of the transition temperature by the rare-earth solute to the lowering of the free energy of the normal state by the polarized spins give a reasonable interpretation of the data.

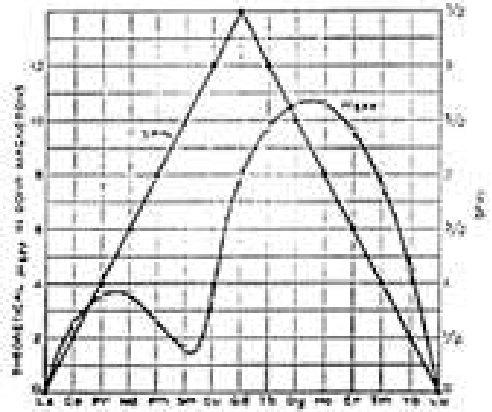

FIG. 2. Effective magnetic moments and spins of the rare earth elements[104].

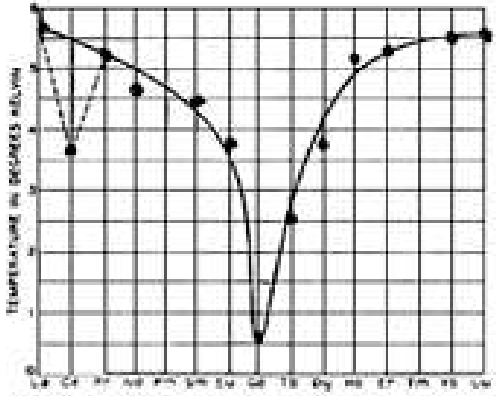

FIG. 3. Superconducting transition temperatures of 1 at. % rare earth solid solutions in La[112].

Transition–nontransition elements. The superconducting transition temperature is always lowered by the formation of solid solutions between transition and nontransition elements, regardless of how N varies. For example, the transition temperature of Nb is increased by solid-solution formation with any transition element with $N < 5$. The addition of Zr ($N = 4$) raises the transition temperature to about 11°K for a solid solution containing 20 to 30 at. % Zr,[104] whereas the addition of Sn ($N = 4$) lowers the transition temperature to 5.6°K for a solid solution containing 5 at. % Sn.[81]

2. *Intermediate Phases*

Nontransition elements. The variation of transition temperature with composition has been studied for

[111] B. T. Matthias, H. Suhl, and E. Corenzwit, Phys. Rev. Letters 1, 92 (1958).
[112] B. T. Matthias, H. Suhl, and E. Corenzwit, J. Phys. Chem. Solids 13, 156 (1960).
[113] J. H. Van Vleck, *The Theory of Electric and Magnetic Susceptibilities*, (Oxford University Press, London, 1932), p. 281.
[114] W. Baltensperger, Helv. Phys. Acta 32, 197 (1959).
[115] H. Suhl and B. T. Matthias, Phys. Rev. Letters 2, 5 (1959).
[116] A. Marshudin and J. Peretti, Compt. Rend. 248, 2650 (1959).

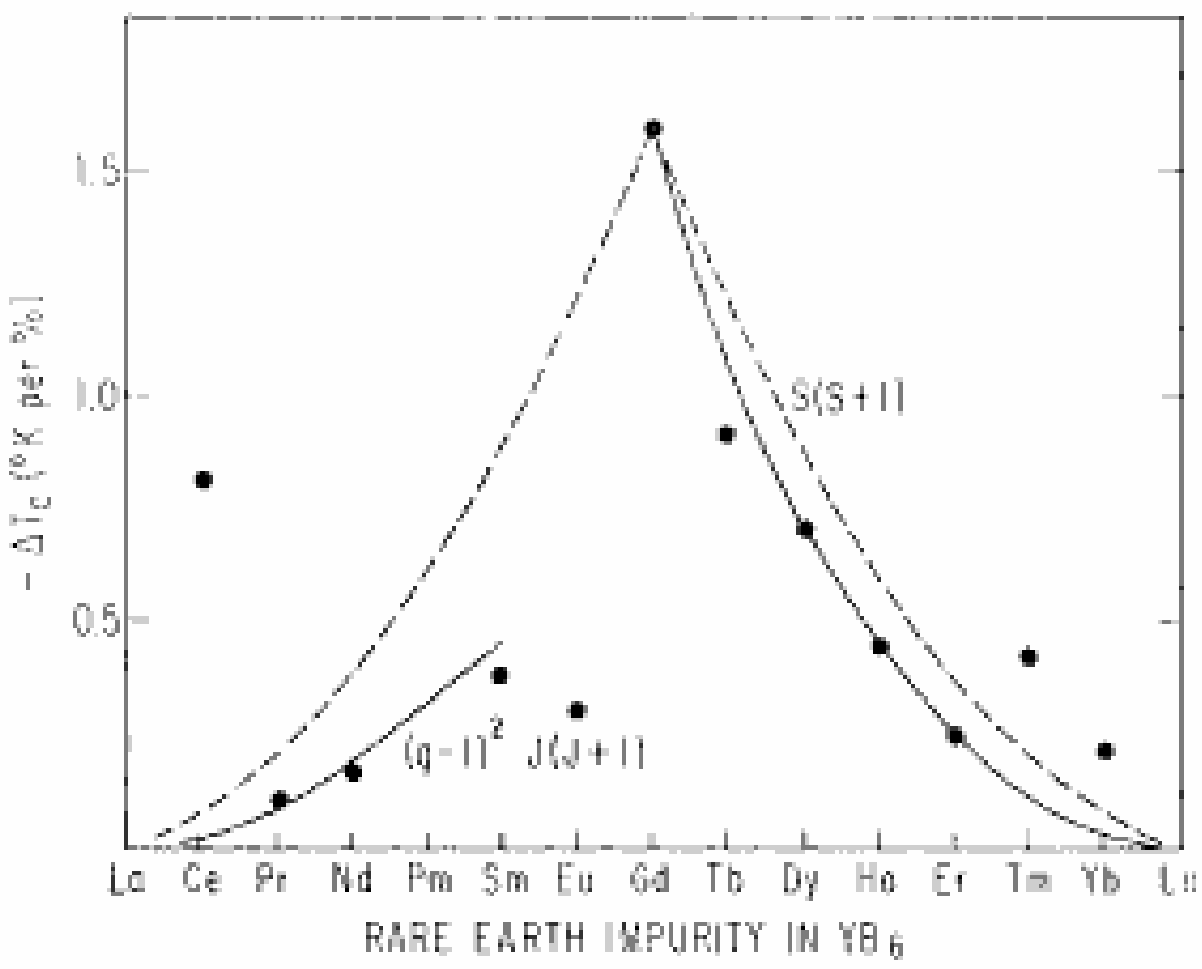

FIG. 1.—Depression of the superconducting transition temperature of YB_6 by 1 atomic per cent addition of rare earth for Y.

Kondo to dense Kondo

- Ce often acts like an impurity in dense Kondo limit
- Yb materials can be in this limit

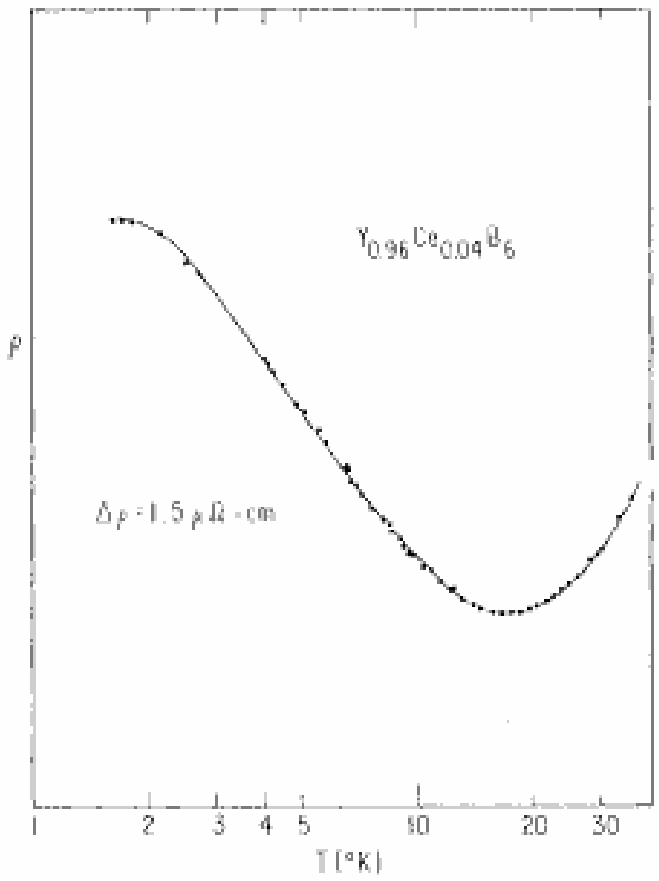

FIG. 2.—Electrical resistance of $Y_{0.96}Ce_{0.04}B_6$ plotted against log T. The abscissa is labeled with temperatures in °K. The ordinate zero is arbitrary; the depth of the minimum is 1.5 $\mu\Omega$-cm, which is roughly 10% of the residual resistivity.

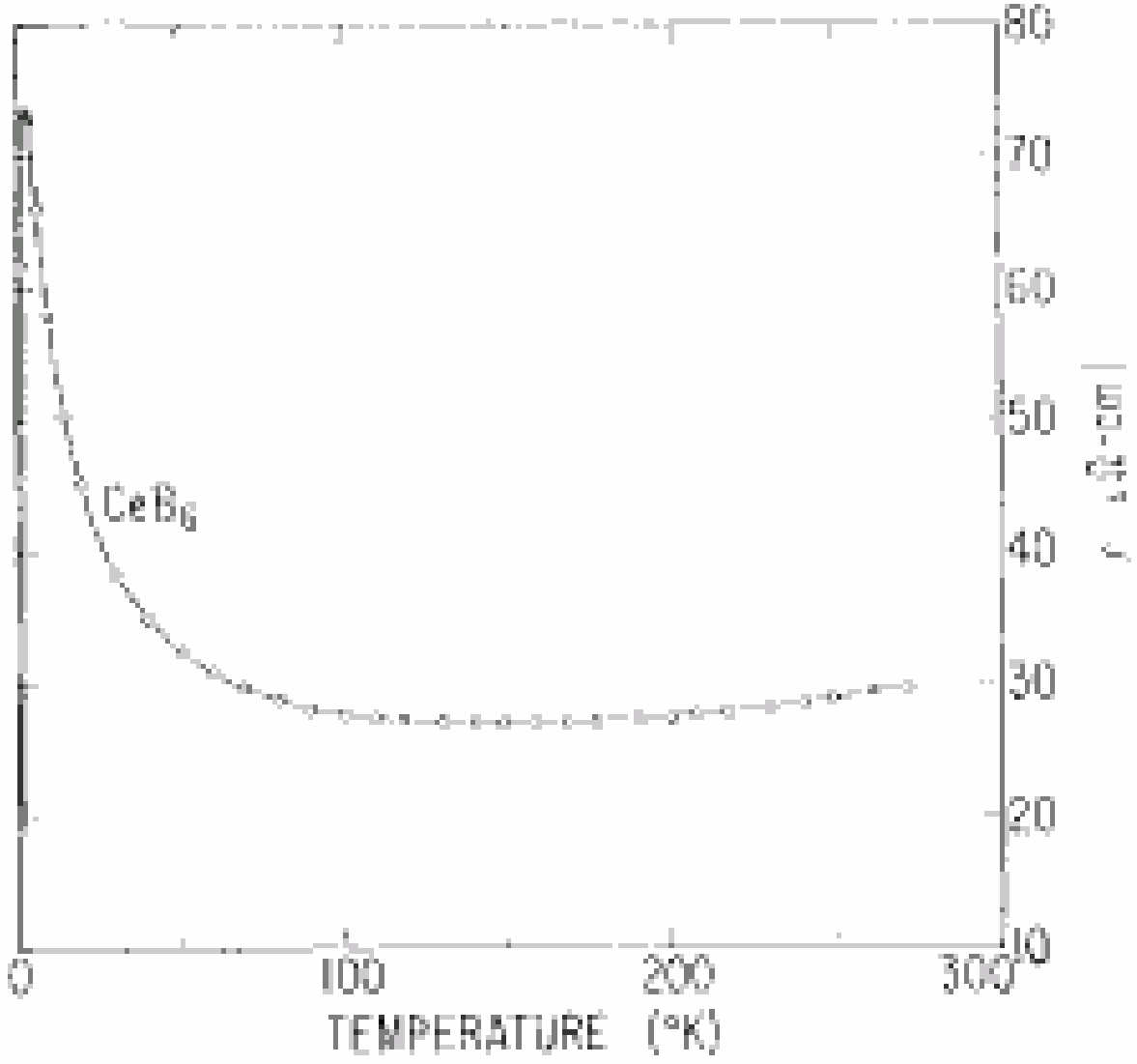

FIG. 3.—Temperature dependence of the electrical resistivity of CeB_6.

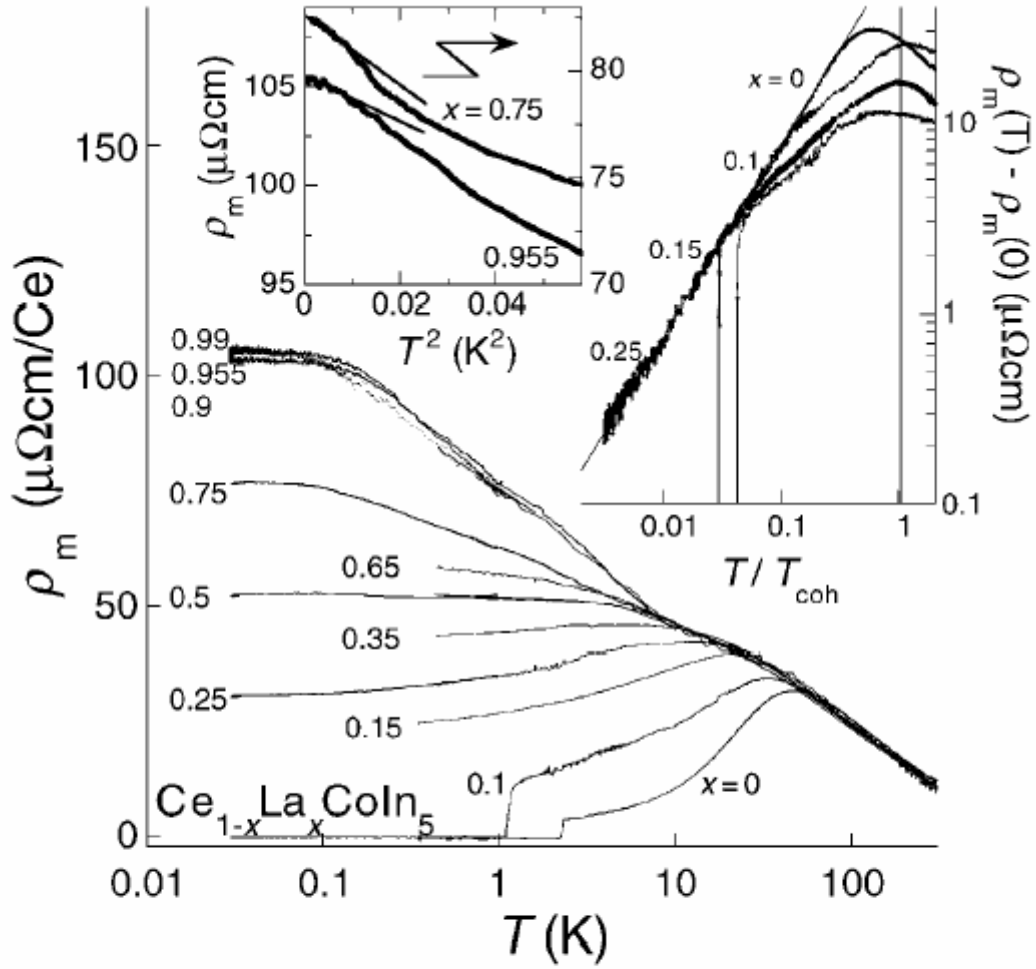

FIG. 1. Magnetic in-plane resistivity ρ_m for various x of $Ce_{1-x}La_xCoIn_5$. Right inset: The log-log plot for the inelastic part of ρ_m vs T/T_{coh}; the solid line is the T linear fit and the vertical lines mark the onset of superconductivity. Left inset: ρ_m vs T^2 for the incoherent regime.

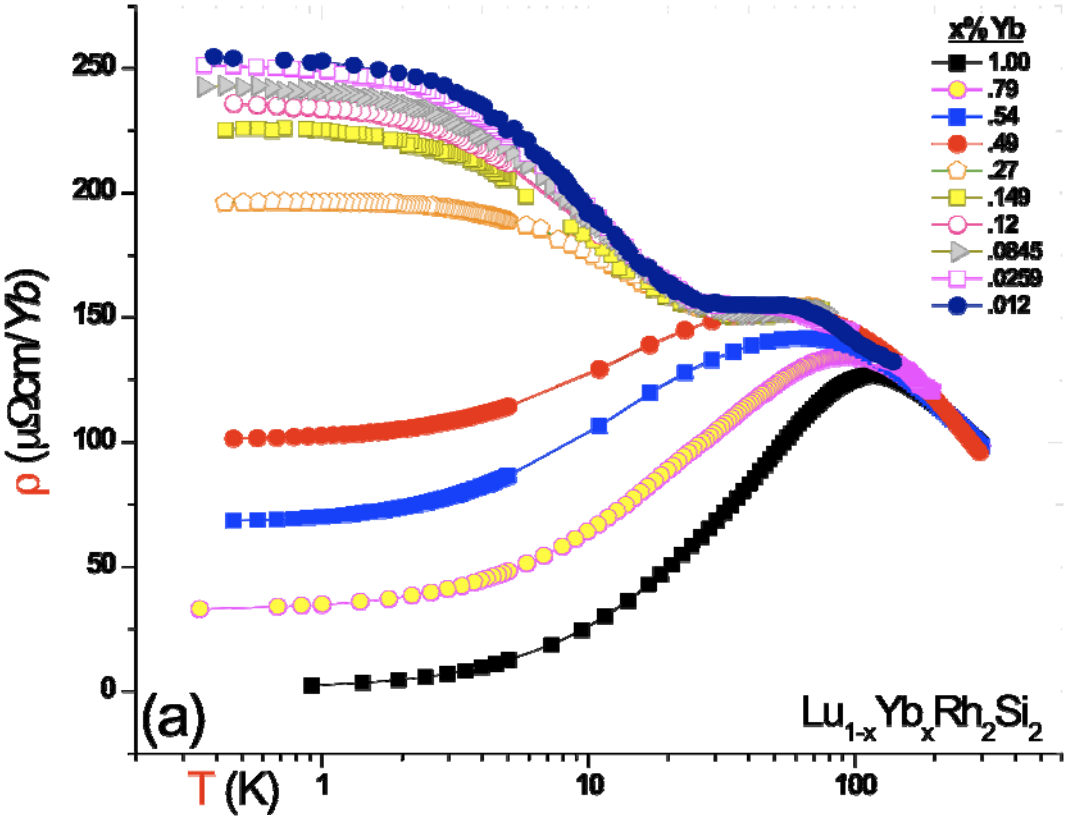
x% Yb
1.00
.79
.54
.49
.27
.149
.12
.0845
.0259
.012
ρ (μΩcm/Yb)
250
200
150
100
50
0
(a)
Lu1-xYbxRh2Si2
T (K)
1
10
100

Intermediate valence

- Doniach phase diagram
- Volume collapse
- Property of coherence

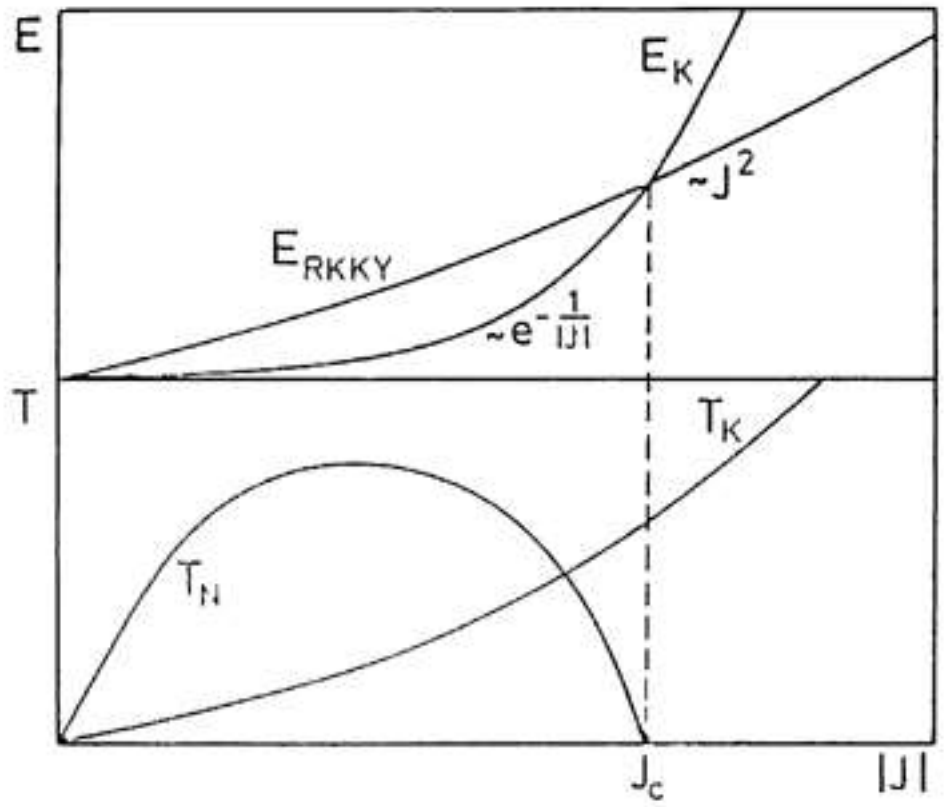

top - Dependences of the characteristic energies connected to the Kondo effect and the RKKY interactions as function of the coupling constant J.
below - Connected "phase diagram".

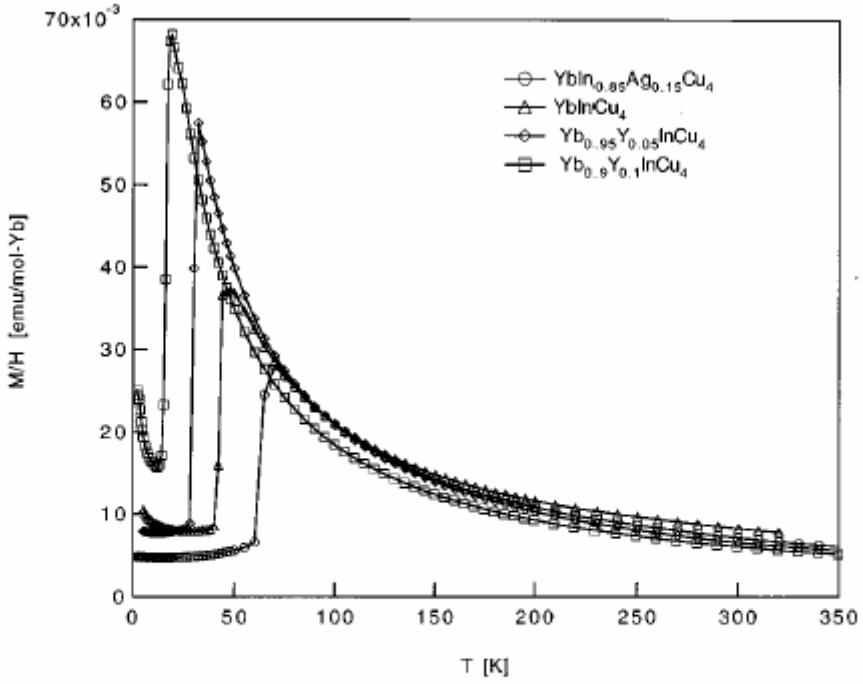

FIG. 1. Magnetic susceptibility versus temperature for representative samples used in this study. Note the sharp drop in susceptibility at the valence transition. The lines are guides to the eye, and the small upturns at lowest temperature for some samples are extrinsic Curie tails.

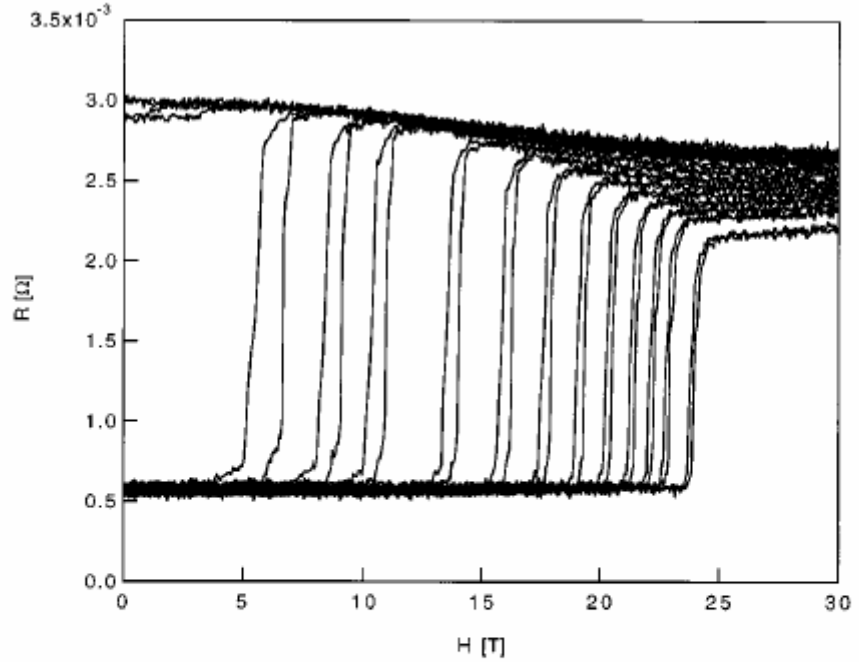

FIG. 2. Resistance as a function of applied field at various fixed temperatures for $YbInCu_4$ under an applied pressure of 6 kbar. Field sweeps were performed at 5, 10, 12, 14, 16, 18, 20, 22, 24, 26, 27, 28, 29, and 30 K (in order of decreasing transition field). At a given temperature, data for both increasing and decreasing field sweeps are shown. The valence transition occurs at higher field for positive field sweeps.

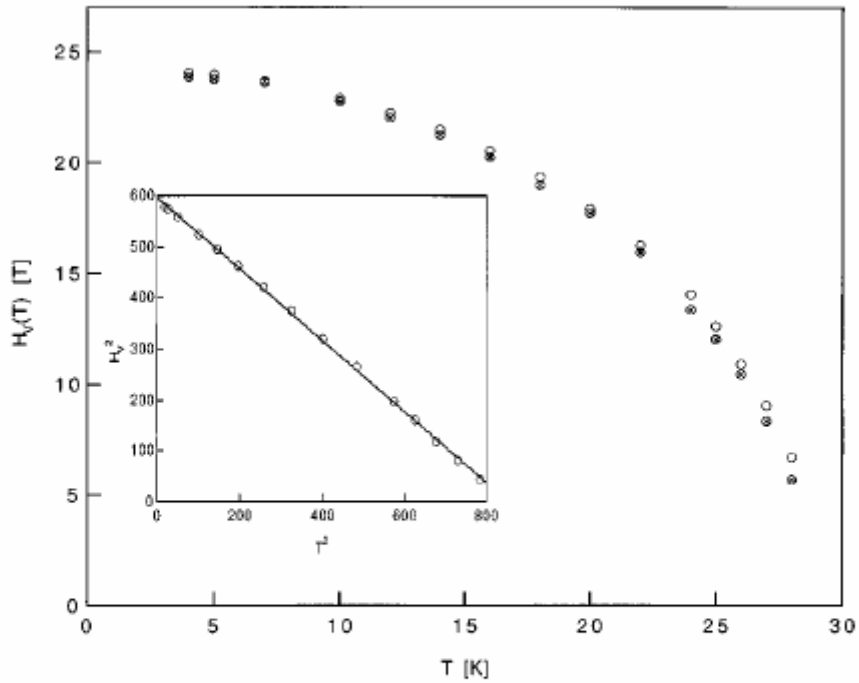

FIG. 3. H_V^+ (open symbols) and H_v^- (filled symbols) as a function of temperature, extracted from the data of Fig. 2. See text for details. The inset shows the linear relationship between H_v^2 (for clarity, only the the H_v^+ data are plotted) and T^2.

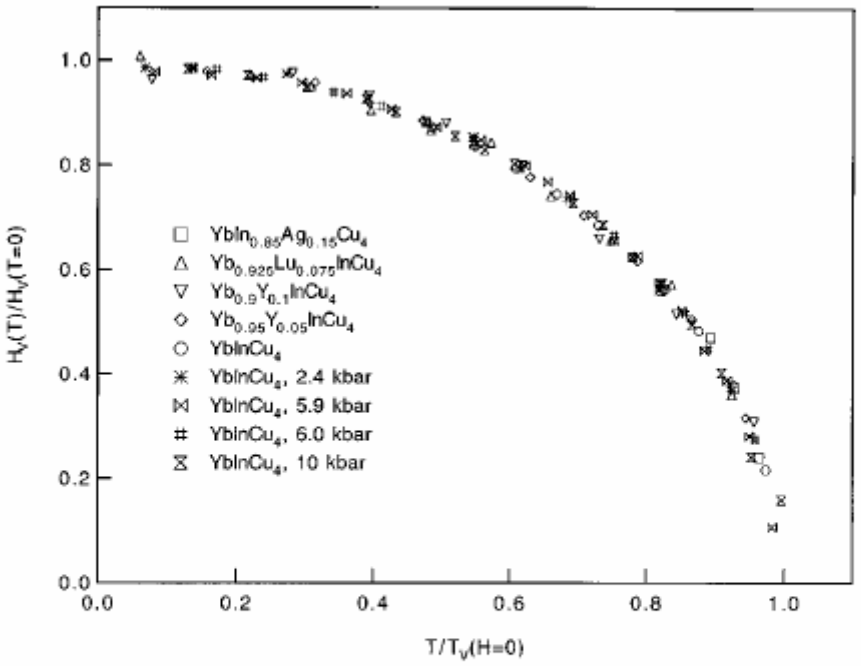

FIG. 4. $H_v(T)/H_v(T=0)$ versus $T_v(H)/T_v(H=0)$ for a variety of samples. The (H_v, T_v) data for a given sample can be collapsed to a universal curve by proper scaling. The data for $YbInCu_4$ at 6.0 kbar were taken with a different crystal than all of the other $YbInCu_4$ data which were obtained with the same crystal.

For $YbInCu_4$ $T_K^U \simeq 25$ K while $T_K^L \simeq 500$ K, as estimated in [7, 13]. With T_v, the temperature of the 'valence transition', for Yb and its alloys lying in the range 10–100 K and $B_c \sim 50$ T [5, 6], the $F_L(B, T)$ in (1) can be taken as a constant (neglecting the magnetic susceptibility term), while for the $F_U(B, T)$ with the trivalent Yb^{3+} considered as a local free ion, one has:

$$F_U(B, T) = E_0 - T \cdot S(B, T) \tag{2}$$

where the temperature dependence of the energy E_0 of the itinerant band is neglected below T_v (this assumption is discussed in more detail below). Correspondingly, the first-order transition line in the (B, T) plane is given by the equation:

$$T \cdot S(B, T) = const \tag{3}$$

where the entropy is determined by the Yb^{3+} multiplet structure only.

The magnetic susceptibility $\chi(T)$ of $YbInCu_4$ above $T_{v0} = 42$ K follows the Curie–Weiss law with an effective moment only negligibly (by 5%) smaller than the whole $J = 7/2$ ground-state moment [6, 13]. Thus, we first neglect the crystal splitting and write:

$$T \cdot S(B, T) = -T \ln \left\{ \sum_{m=-J}^{J} \exp\left(-\frac{g_J \mu_B B}{T} m \right) \right\} \tag{4}$$

where g_J is a g-factor (for $J = 7/2$, $g_J = 8/7$). From (4) the relation $a \mu_B B_{c0} = T_{v0}$ between the critical field B_{c0} at $T = 0$ and the value of the structural transition temperature T_{v0} at zero field, is of the form:

$$g_J J \mu_B B_{c0} = T_{v0} \ln (2J + 1) \tag{5}$$

which gives $a \approx 1.9$ for $J = 7/2$, a result which is remarkably close to the experimental value $a \simeq 1.8$ [6].

Fig. 1

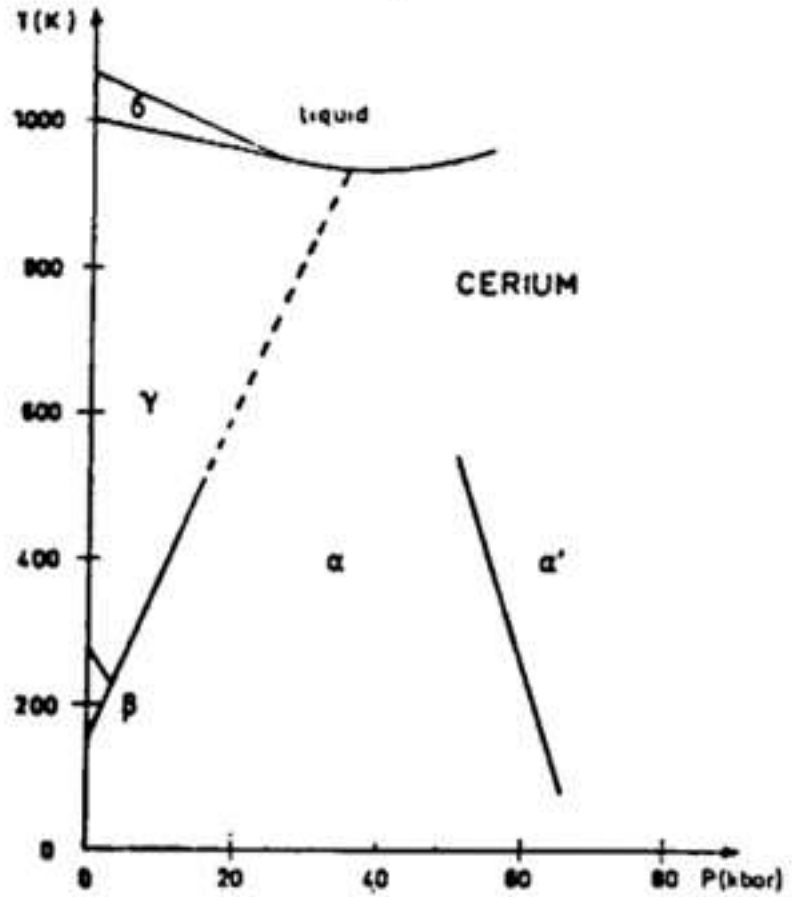

The phase diagram of cerium (δ = b.c.c., γ = f.c.c., β = *dhcp*, α = f.c.c. and α' = f.c.c. or distorted *dhcp*). The extension of the true α–γ transition line meets the minimum point of the melting curve.

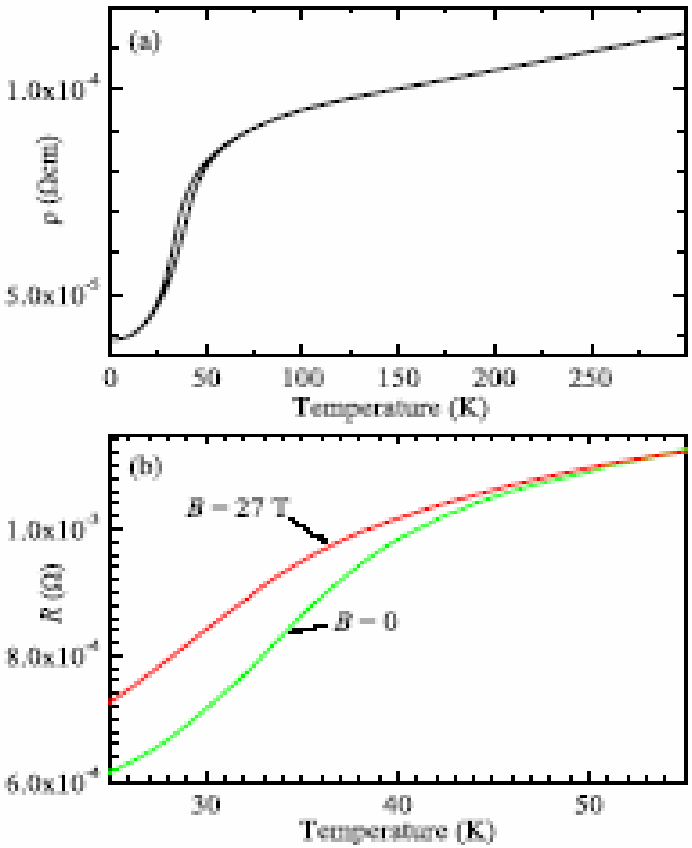

Figure 1. (a) Resistivity ρ of $Ce_{0.8}La_{0.1}Th_{0.1}$ as a function of temperature T with applied magnetic field $B = 0$. The data are recorded by sweeping T at $\sim$1 K min^{-1} from 300 to 2 K and then back to 300 K. Note the hysteresis between down- and up-sweeps of T close to the transition. (b) Resistance R of a $Ce_{0.8}La_{0.1}Th_{0.1}$ sample versus T at $B = 0$ and 27 T. In each case, the sample is warmed above 200 K and then cooled at $\sim$1 K min^{-1} in the stated field.

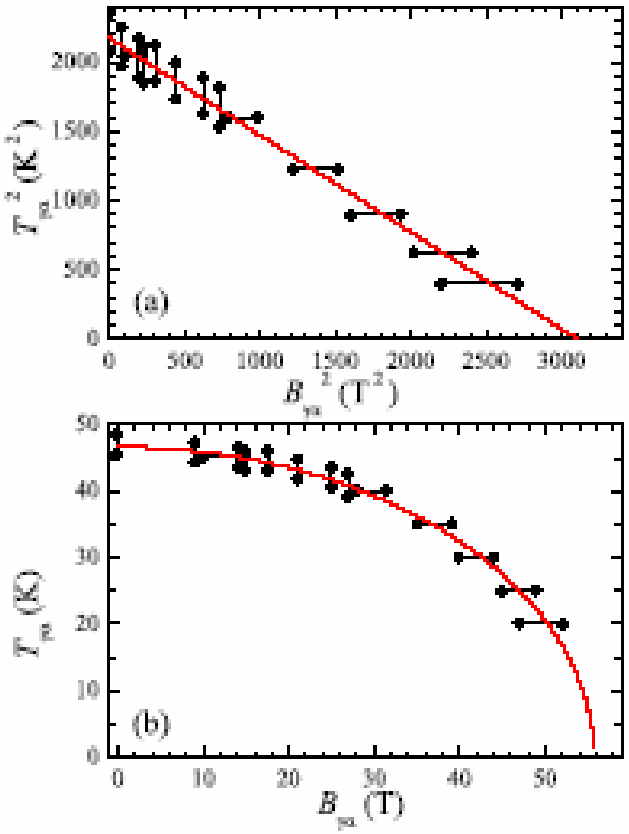

Figure 3. Values of $B_{p\alpha}(T)$ from the $M(B)$ experiments at fixed T (horizontal error bars) and values of $T_{p\alpha}(B)$ from $\rho(T)$ experiments at fixed B (vertical error bars) plotted as T^2 versus B^2 (a) and in linear units (b). The line in (a) and the curve in (b) represent equation (2) with $B_{p\alpha}(T \to 0) = 56$ T and $T_{p\alpha}(B = 0) = 46.6$ K.

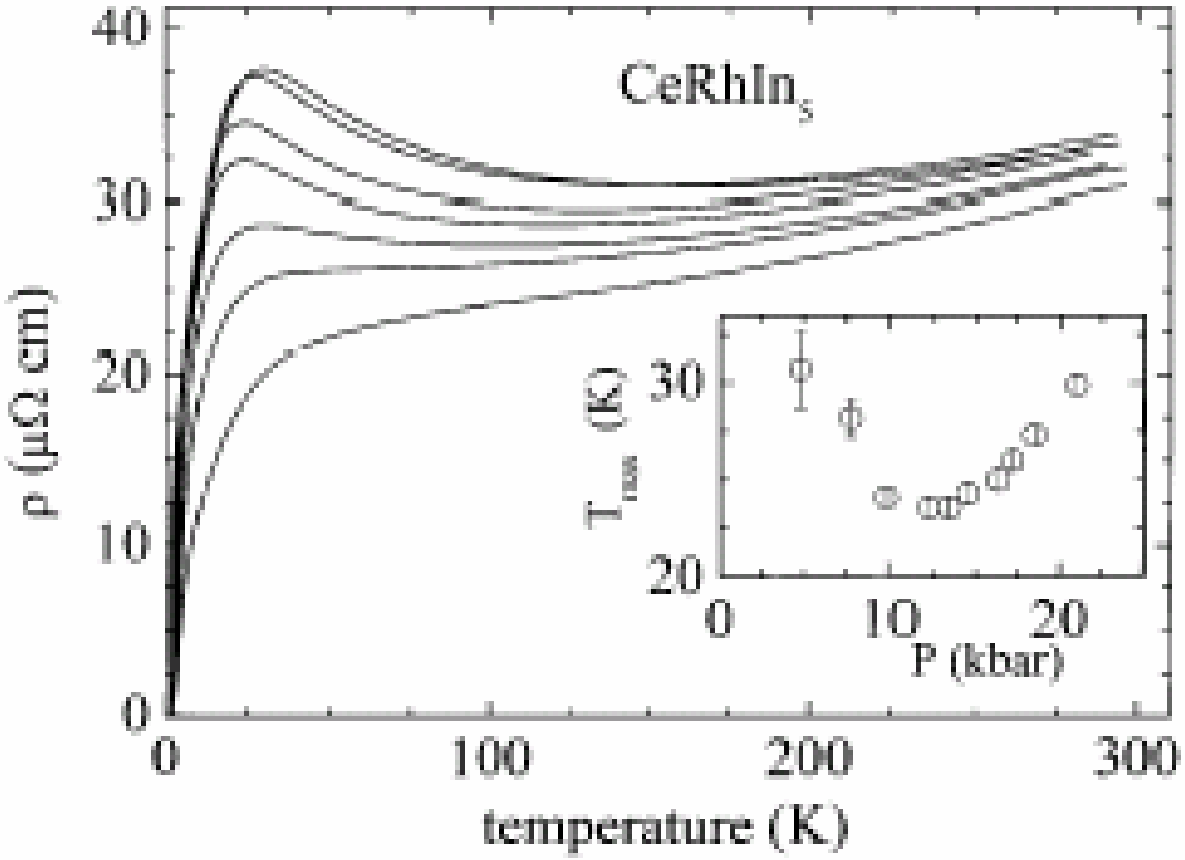

FIG. 2. Temperature dependence of the electrical resistivity of $CeRhIn_5$ at representative applied pressures. Data shown correspond to pressures of 0.001, 4.8, 7.9, 12.2, 14.5, 18.5, and 21.0 kbar and are associated, respectively, with curves of increasing resistivity at 50 K. The inset is a plot of the pressure dependence of the temperature T_{max} where the resistivity is a maximum.

4f to 5f

- Lanthanide contraction
- Kondo effect in U-based materials
- 5f dense Kondo behavior
- $PuCoIn_5$

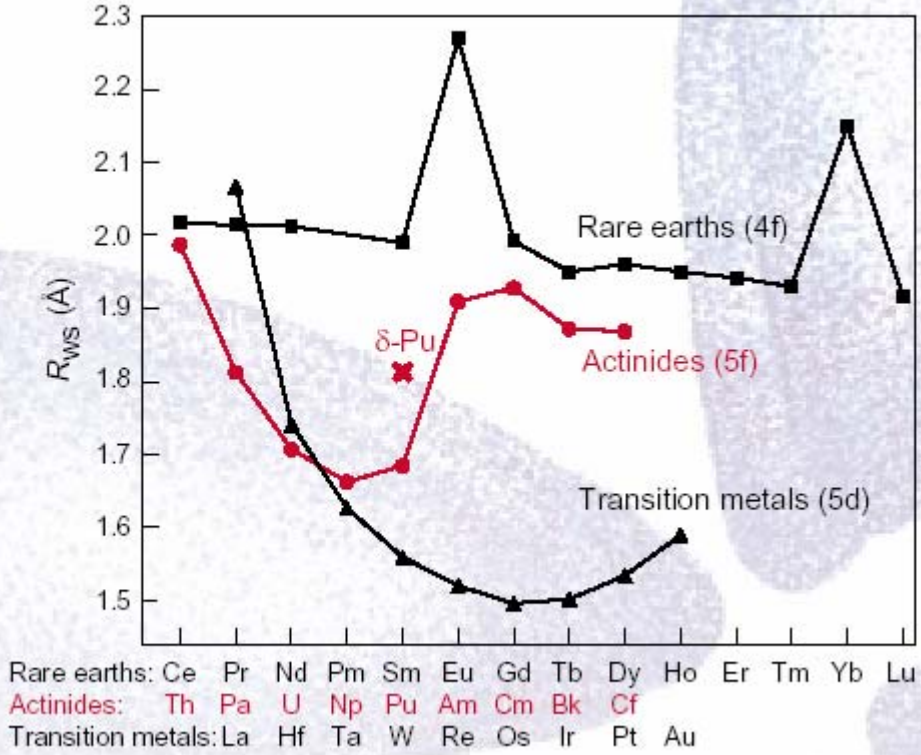

The atomic radii of the actinide metals are compared with those of the rare earths and transition metals.

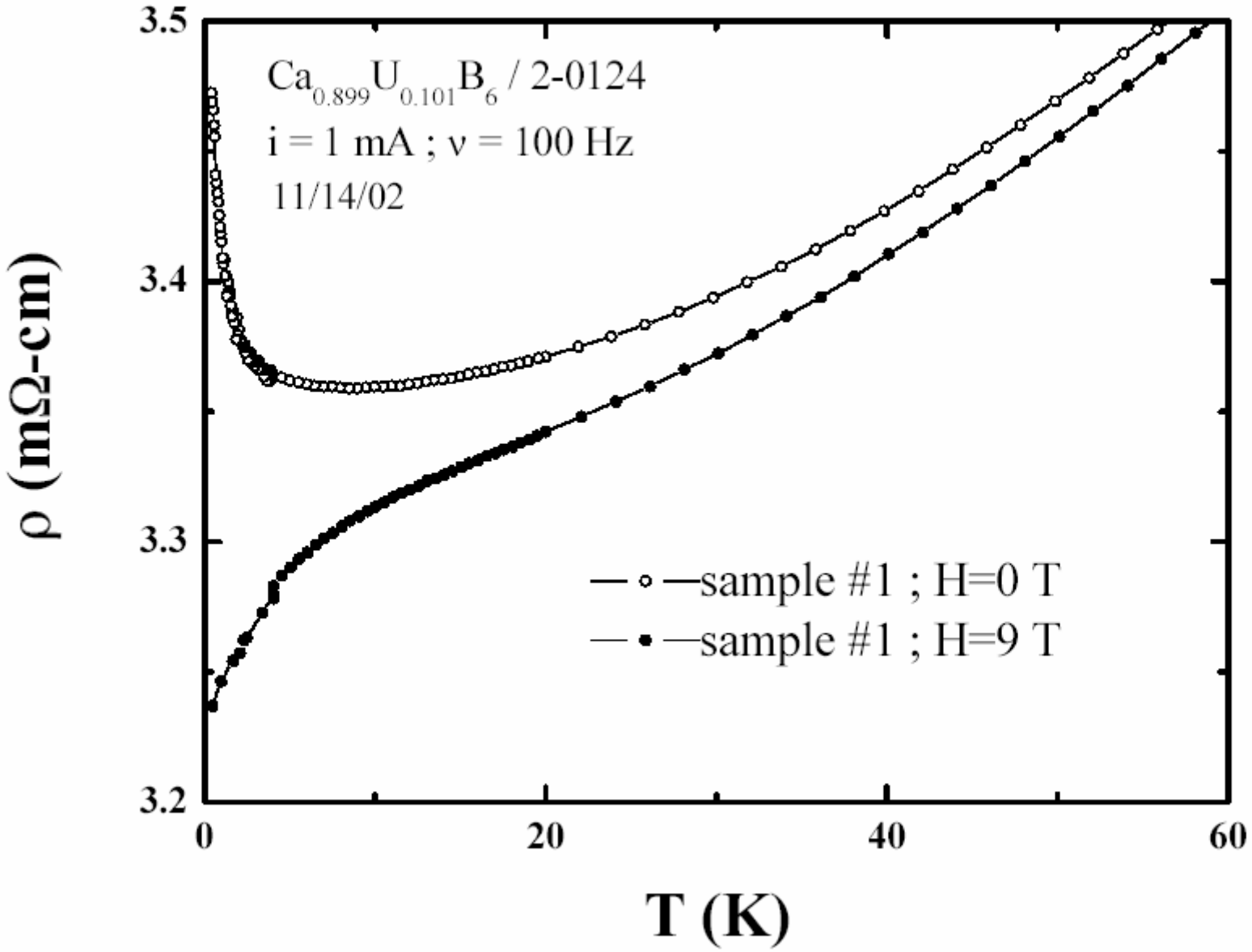
3.5
3.4
3.3
3.2
0
20
40
60
ρ (mΩ-cm)
T (K)
Ca0.899U0.101B6 / 2-0124
i = 1 mA ; ν = 100 Hz
11/14/02
—○—sample #1 ; H=0 T
—●—sample #1 ; H=9 T

Takagi & Suzuki JPSJ 68(1999)3693

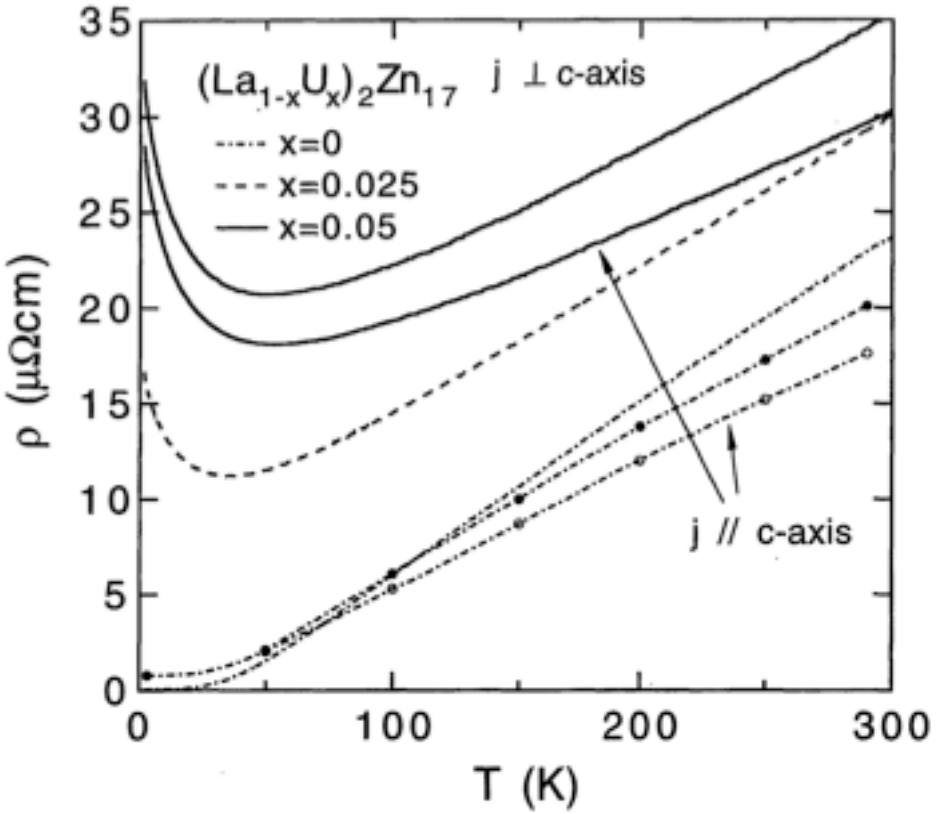

Kondo effect in U-doped La_2Zn_{17}

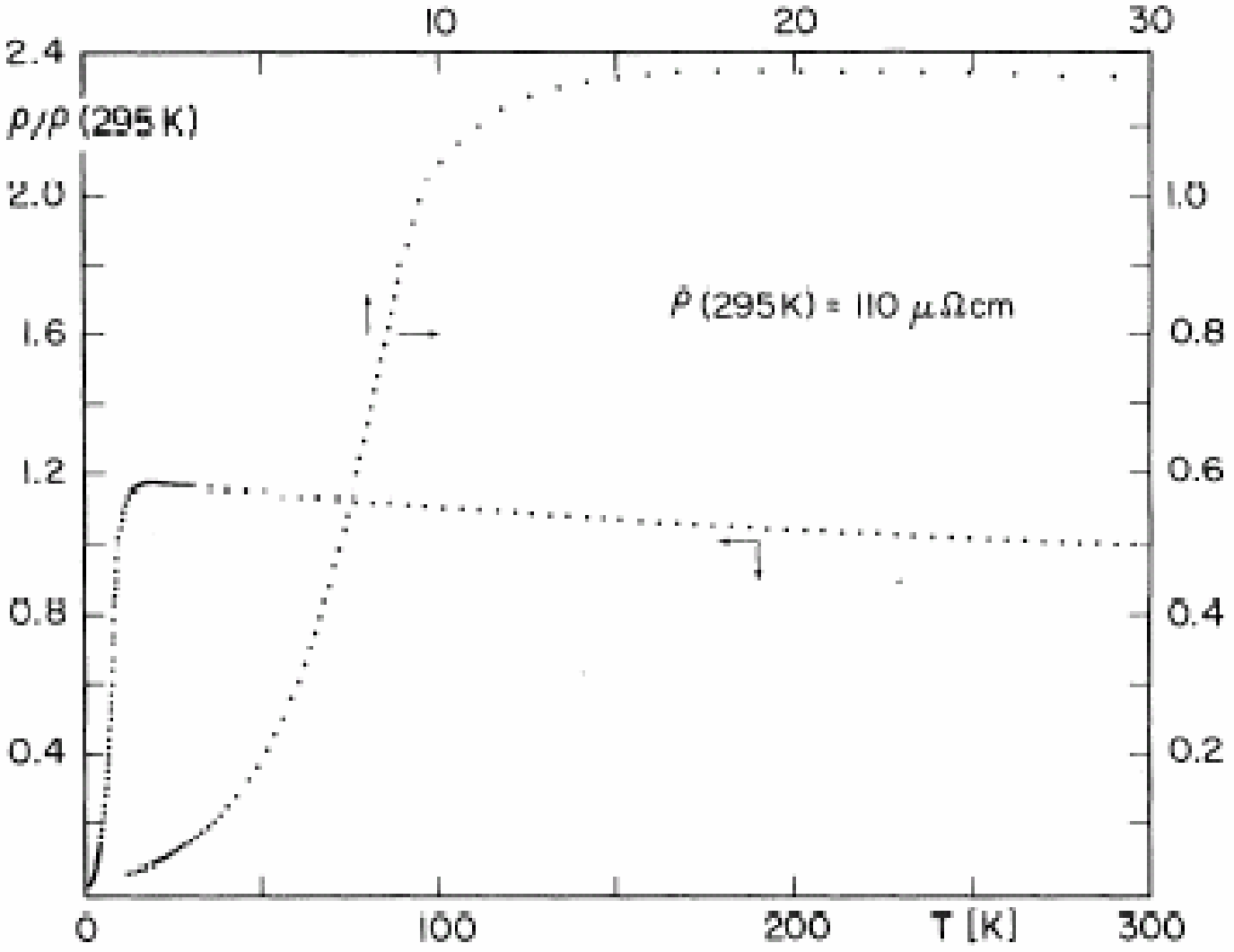

FIG. 3. Temperature dependence of the electrical resistivity of U_2Zn_{17} between 1.2 and 300 K. Note the different scales for different temperature intervals.

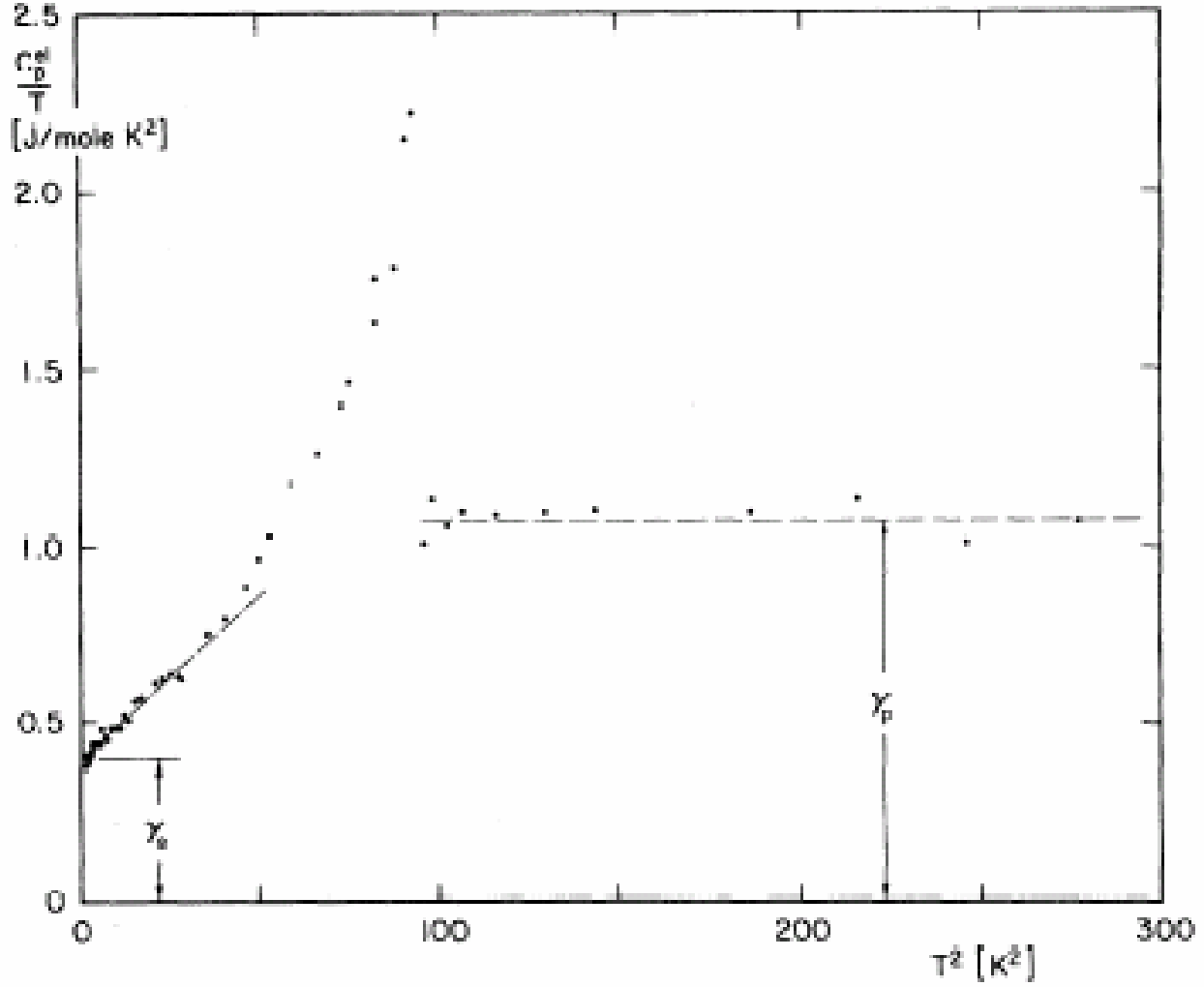

FIG. 2. Upper part, temperature dependence of the specific heats of U_2Zn_{17} and Th_2Zn_{17} between 1.5 and 18 K. Lower part, specific heat minus the lattice contribution of U_2Zn_{17} at low temperatures.

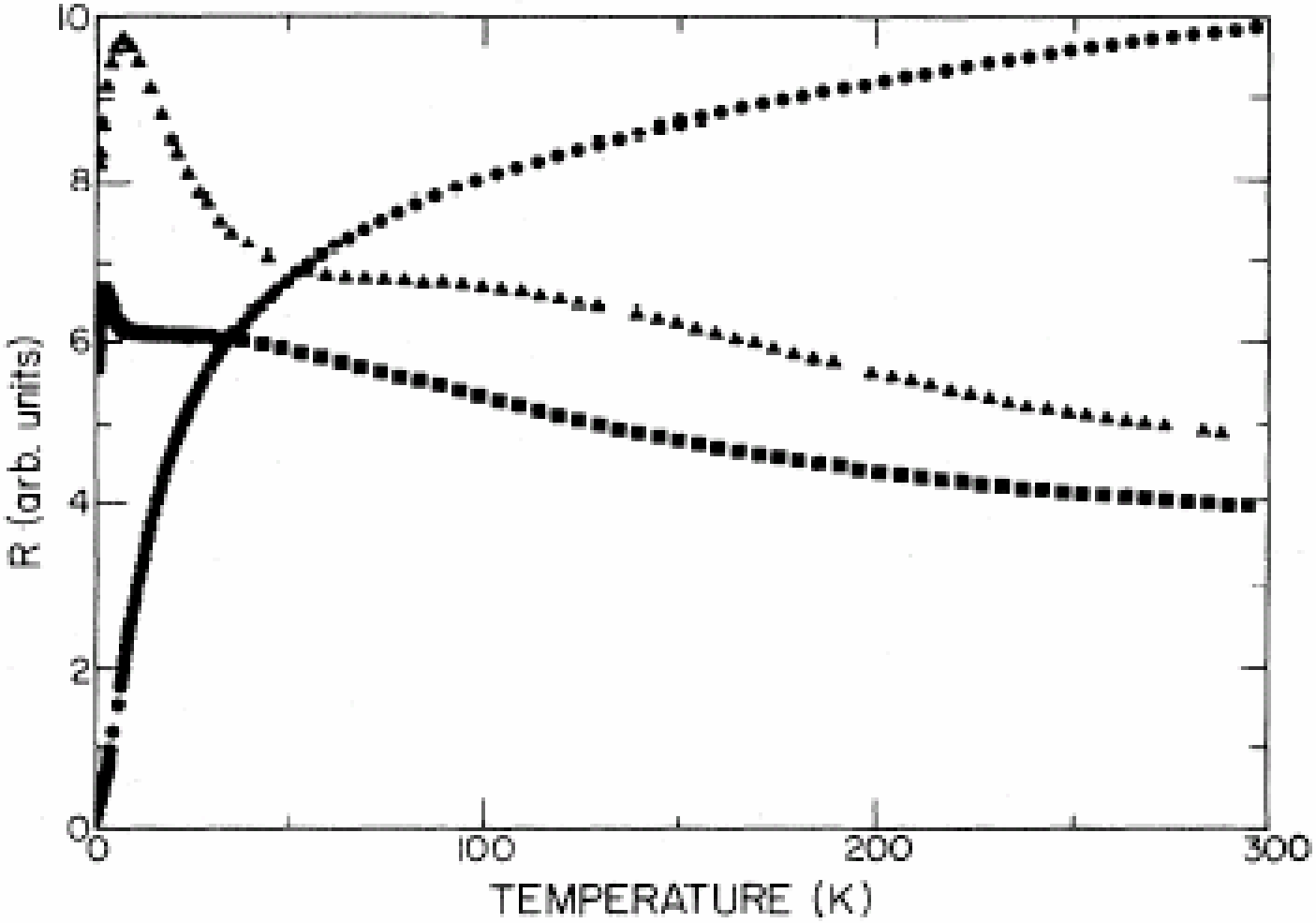

FIG. 3. Resistance vs temperature of $CeCu_2Si_2$ (triangles), UBe_{13} (squares), and UPt_3 (dots). Note the similarity of the data for the first two—both have low-temperature peaks and shoulders at higher temperature.

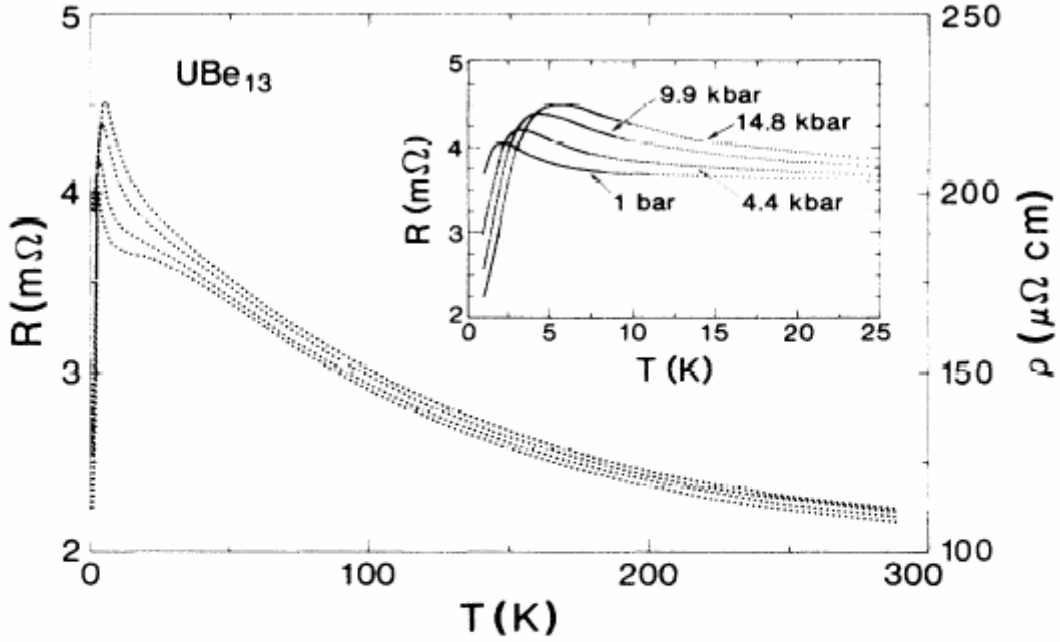

FIG. 1. Electrical resistance R and resistivity ρ versus temperature T of UBe_{13} at pressures of 1 bar, 4.4, 9.9, and 14.8 kbar. The inset provides an expanded view of these curves below 25 K.

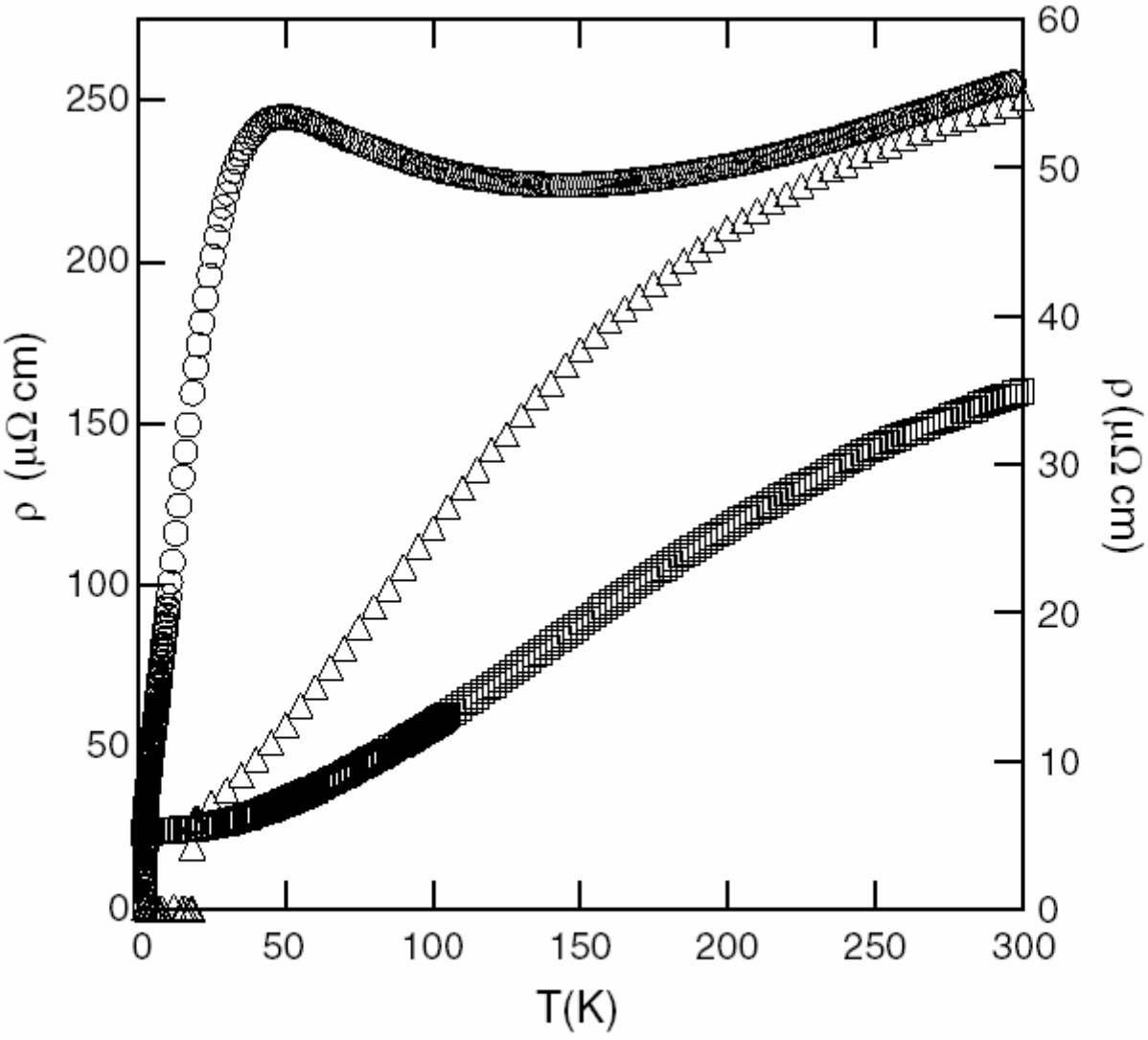

Figure 2. Resistivity as a function of temperature for $CeCoIn_5$ (circles), $PuCoGa_5$ (triangles), and $UCoGa_5$ (squares). The data for $CeCoIn_5$ are plotted using the right axis, whereas $PuCoGa_5$ and $UCoGa_5$ use the left.

Kondo Insulators and Zintl compounds

- 4f/5f examples
- 3d examples
- electron precise compounds
- ionic/metallic border

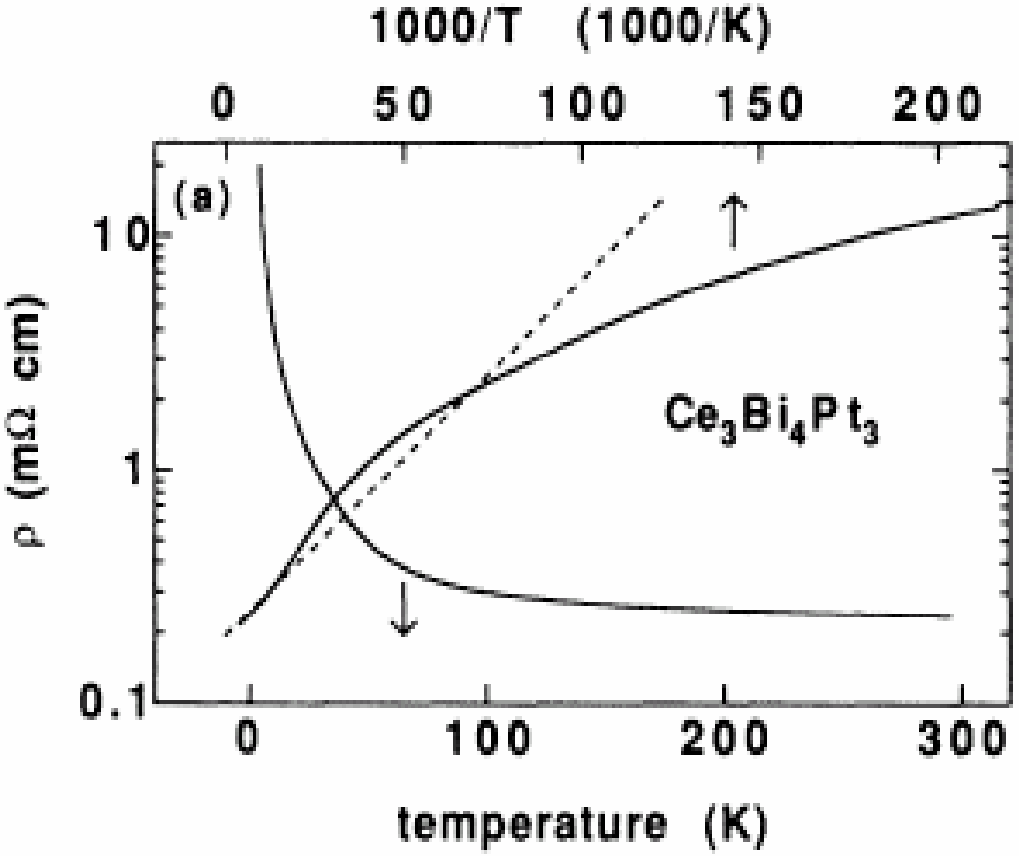
1000/T (1000/K)
0
50
100
150
200
(a)
10
1
0.1
ρ (mΩ cm)
Ce3Bi4Pt3
0
100
200
300
temperature (K)

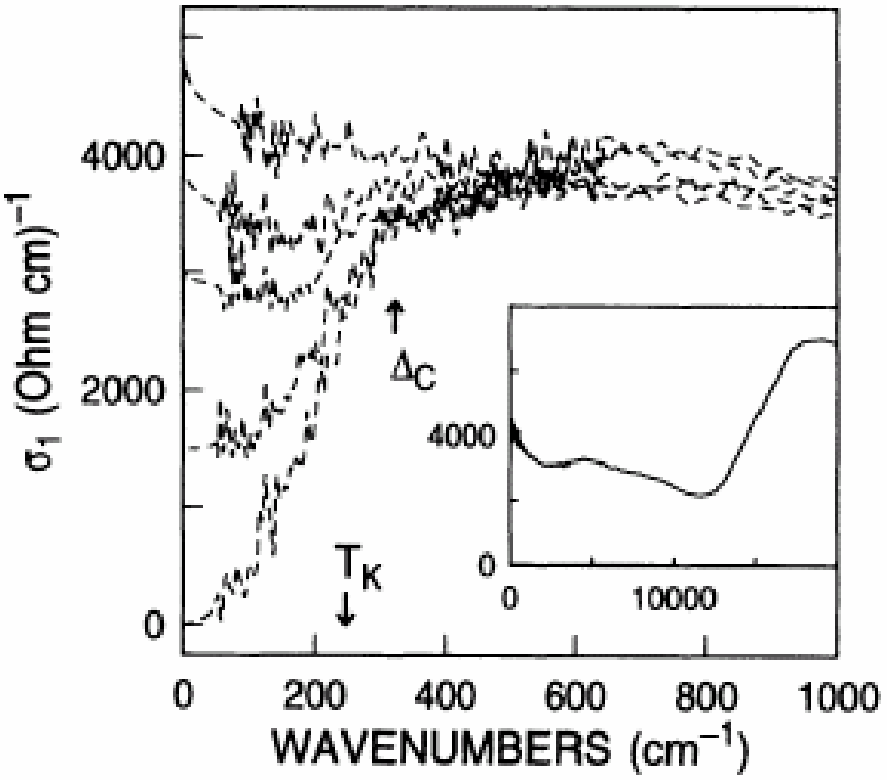

FIG. 2. Real part of the optical conductivity $\sigma_1(\omega)$ for different temperatures (from below: 25, 50, 75, 100, and 300 K). A gap is opening below 100 K; the prominent feature at Δ_c seems to be independent of temperature. The inset presents the optical region of σ_1.

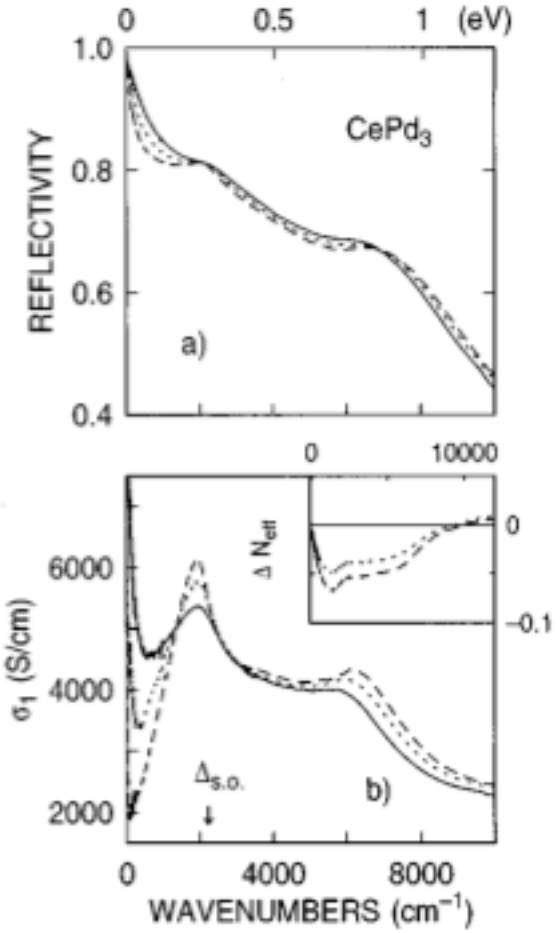

FIG. 2. (a): Reflectivity of $CePd_3$ at 250 K (solid), 150 K (dotted), and 25 K (dashed). The spectra below 75 K and above 2000 cm^{-1} nearly coincide. (b) Optical conductivity of $CePd_3$ at 250, 150, and 25 K. Spectral weight below 1000 cm^{-1} shifts to higher energy. The inset shows ΔN_{eff} as calculated by Eq. (1) (see text) for temperatures of 150 K (dotted) and 25 K (dashed).

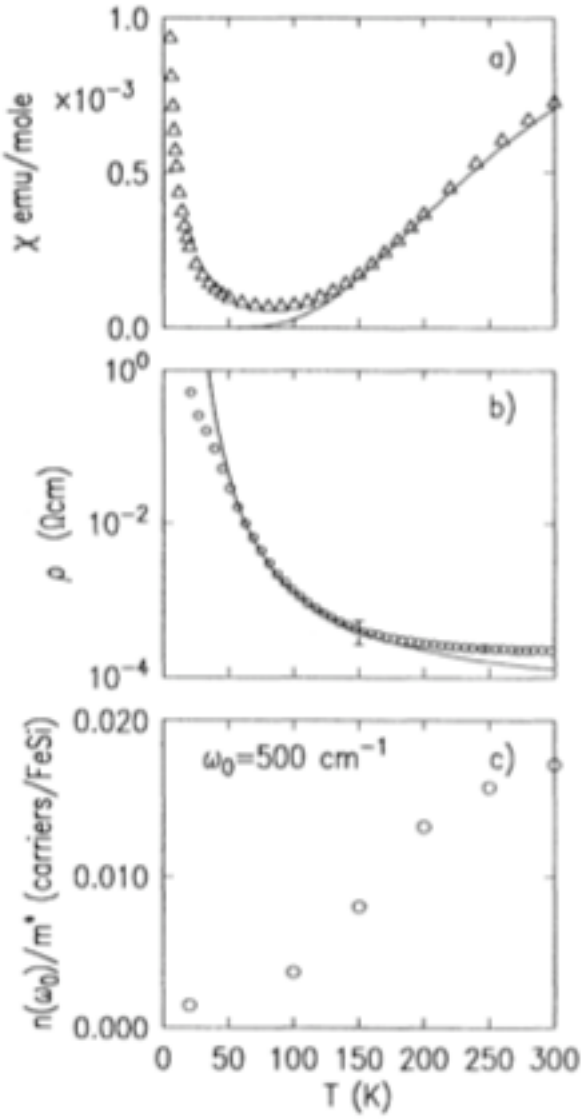

FIG. 1. Magnetic susceptibility χ, the resistivity ρ, and the integral of the infrared conductivity from 0 to 500 cm^{-1}, n/m^*, are shown as a function of temperature for cubic FeSi. The solid curves in parts (a) and (b) are activated forms, as described in the text.

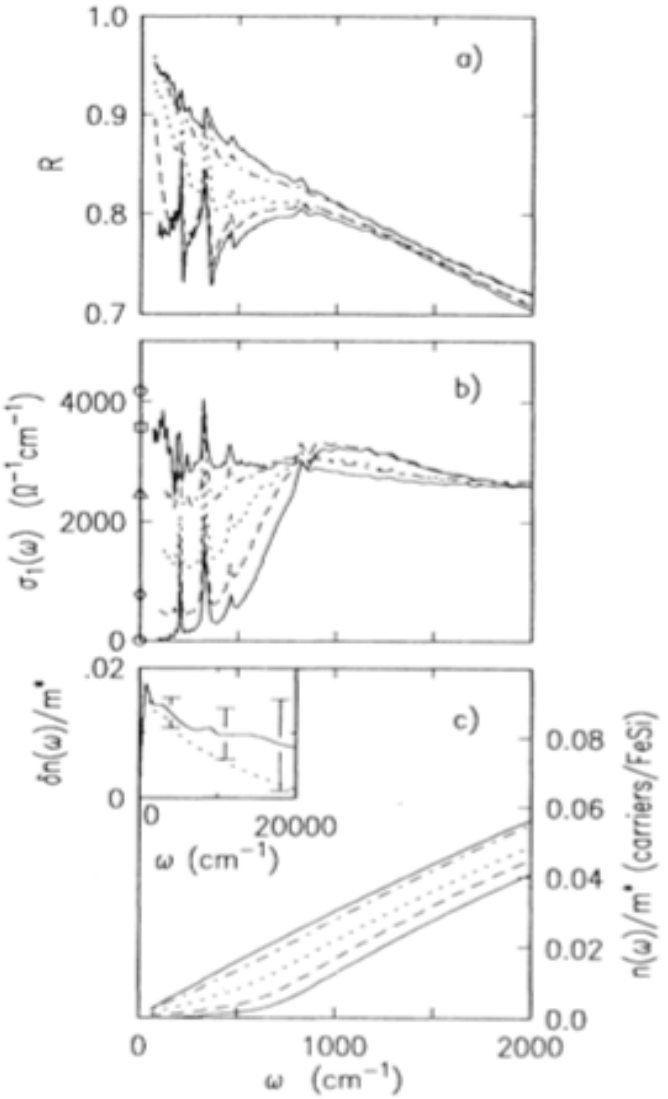

FIG. 3. Infrared reflectivity R, conductivity $\sigma_1(\omega)$, and the integral of the conductivity from 0 to ω, $n(\omega)/m^*$, are shown as a function of frequency for $T=20$ (solid), 100 (dashed), 150 (dotted), 200 (dot-dashed), and 250 K (solid) for cubic FeSi. The symbols at $\omega=0$ show the measured values of σ_{dc} [from Fig. 1(b)] for the same temperature sequence. The inset shows the difference between $n(\omega)/m^*$ at 250 and at 20 K (solid curve). The dotted curve shows the effect on $n(\omega)/m^*$ shifting the 20 K reflectivity data by +0.5%.